Sequence-encoded grammars determine material properties and physical aging of protein condensates

Ibraheem Alshareedah[1,§], Wade M. Borcherds[2,§], Samuel R. Cohen[3,4,§], Mina Farag[3], Anurag Singh[1], Anne Bremer[2], Rohit V. Pappu[3,*], Tanja Mittag[2,*], Priya R. Banerjee[1,*]

[1]Department of Physics, The State University of New York at Buffalo, Buffalo, NY 14260, USA
[2]Department of Structural Biology, St. Jude Children's Research Hospital, Memphis, TN 38105, USA
[3]Department of Biomedical Engineering and Center for Biomolecular Condensates, Washington University in St. Louis, St. Louis, MO 63130, USA
[4]Center of Regenerative Medicine, Washington University in St. Louis, St. Louis, MO 63130, USA

§Equal contributions

*Corresponding authors. pappu@wustl.edu; tanja.mittag@stjude.org; prbanerj@buffalo.edu;

Abstract

We demonstrate that nascent versus aged condensates formed by prion-like low complexity domains (PLCDs) are distinct types of viscoelastic materials. Nascent PLCD condensates are terminally viscous Maxwell fluids whose viscoelastic moduli are governed by the strengths of aromatic stickers. Upon physical aging, PLCD condensates transition, on sequence-specific timescales, from fluids to non-fibrillar, elastic Kelvin-Voigt solids. Accordingly, fluid-like condensates of PLCDs are metastable, whereas elastic solids are the stable material states. Fluid-to-solid transitions are accelerated by mutations to spacers that weaken metastable fluids with respect to stable solids. Evolutionarily selected PLCD sequence features that enhance the metastabilities of fluid-like condensates are likely to render the barriers for conversion from fluids to solids to be insurmountable on timescales that are relevant to cellular processes.

Macromolecular phase transitions [1], which include processes such as phase separation coupled to percolation [2], give rise to compositionally distinct membraneless bodies known as biomolecular condensates [3]. The current thinking is that there is an intimate connection between the material properties of condensates and the functions or pathologies they influence in cells [4-7]. What remains unclear, however, are the rules that connect sequence-encoded interactions to material properties of condensates. Further, while it is known that the material properties of condensates can change as they physically age [4,8-10], it is unclear if the stable states that minimize the global free energy of condensates are elastic solids or viscous liquids. Here, we report results from systematic assessments of the connections between sequence-encoded interactions and time-dependent material properties of condensates.

We focus on condensates formed by intrinsically disordered PLCDs [11-13]. These domains are prominent drivers or modulators of several functionally relevant and pathogenically significant condensates [14-16]. The stickers-and-spacers framework [17] has been useful for modeling and explaining the connections between sequence-encoded information and the driving forces for condensate formation by PLCDs [11-13]. Aromatic residues are cohesive motifs known as stickers that form reversible physical crosslinks [11-13]. Spacers in PLCDs are primarily Gly, Ser, and Gln that affect the solubility and impact the cooperativity of inter-sticker crosslinks [11-13]. Recent coarse-grained simulations reproduced the measured phase behaviors for thirty variants of A1-LCD [13], the PLCD derived from the RNA binding protein hnRNP A1. These computations and recent single fluorogen imaging studies [18] have shown that PLCDs within condensates form physically crosslinked networks with hub-and-spoke like topological structures. Hubs are organized around intermolecular crosslinks among clusters of aromatic stickers [18]. Further, the interplay between sticker- and spacer-mediated effects leads to spatially inhomogeneous organization of PLCD molecules within condensates, and the inhomogeneities span multiple length scales [13,18]. There is also growing recognition that condensates, including those formed by PLCDs, are viscoelastic materials [19-23]. Accordingly, our focus is on understanding how network-like structures within condensates determine their frequency-dependent storage (elastic) and loss (viscous) moduli. The key unanswered question is whether viscoelastic moduli of PLCD condensates are sequence-specific emergent properties that depend on the network structures of condensates. To answer this question, we leverage results from recent simulations for PLCDs [13,24], and compute viscoelastic moduli using a graph-theoretic adaptation [25,26] of Rouse-Zimm theory [27,28].

A key ingredient of the Rouse-Zimm theory is the Zimm matrix, which can be constructed as a graph Laplacian [29]. The diagonal elements of Zimm matrices are the degree, defined as the number of edges incident on a node, where a node is a residue in a chain, and the off-diagonal elements specify the connectivity. The off-diagonal elements are set to –1 if there is an edge between two nodes or 0 if there is no edge. The eigenvalue spectra of Zimm matrices yield computed estimates for dynamical moduli. Elements of the Zimm matrix are typically constructed by accounting for intramolecular physical crosslinks that form as the result of a single chain moving in a medium. Are the dynamics of a single chain in an effective solvent sufficient for explaining measured viscoelastic moduli of PLCD condensates or must one account for details of the network structure of condensates? To answer this question, we computed two versions of the Zimm matrix from published simulation results [13]. In the "single-chain model", the Zimm matrix was computed by accounting for intramolecular crosslinks alone. Conversely, in the "collective model", the ensemble-averaged Zimm matrix was computed using the condensate-spanning network as a single chain.

We compared computed moduli to those measured using passive microrheology with optical tweezers [22] (**Fig. 1a**). These experiments yield the frequency-dependent storage (G') and loss (G'') moduli of a condensate through analysis of the thermal fluctuations of the positions of optically trapped polystyrene particles within the condensate (**Fig. 1b**). The frequency-dependent moduli were calculated via Fourier transformation of the position autocorrelation functions of the beads and the optical trap stiffness [22] (**Fig. 1c**). For condensates formed by WT, storage moduli computed using the single-chain model were overestimates vis-à-vis the measured values (**Fig. 1d** and **ED Fig. 1a, 1b**). In contrast, the storage moduli computed using the collective model showed good agreement with measured values (**Fig. 1e** and **ED Fig. 1a, 1b**). The computed loss moduli were less sensitive to how we computed the Zimm matrix, although the overall agreement was superior when using the collective model (**Fig. 1d, 1e** and **ED. Fig. 1b**). These results establish that storage moduli are emergent properties governed by details of network structures that define how A1-LCD molecules are organized within the condensate. Conversely, loss moduli can be inferred by analyzing the relaxation modes of individual molecules.

In addition to highlighting the emergent nature of storage moduli, the measured and computed moduli show a set of distinct features (**Fig. 1f**): There exists a crossover frequency ($\omega_{crossover}$) such that $G' < G''$ below $\omega_{crossover}$ and $G' > G''$ above $\omega_{crossover}$. This points to dominantly viscous behaviors at long timescales whereas elastic behaviors dominate at short timescales. Further, the storage modulus plateaus above $\omega_{crossover}$, and varies as ω^2 below $\omega_{crossover}$. The loss modulus varies linearly with ω below $\omega_{crossover}$, and as ω^{-1} above $\omega_{crossover}$. The presence of a single crossover frequency and the specific functional forms we extract for the frequency dependencies above and below $\omega_{crossover}$ imply that nascent condensates formed by wild-type A1-LCD are viscoelastic Maxwell fluids [19,22].

Next, we asked if nascent condensates formed by different variants of A1-LCD are also Maxwell fluids (**ED Fig. 1c, 1d**) and whether their viscoelastic moduli were determined by sticker types. In these variants, the aromatic stickers of A1-LCD were replaced by Phe (allF), Tyr (allY), or Trp (allW). We also studied variants where only Phe (FtoW) or Tyr (YtoW) residues were replaced by Trp. Finally, in the variant W-, all stickers were Trp residues, and the number of stickers was reduced by a factor of 0.35. Aromatic stickers follow a hierarchy of strengths whereby Trp is the strongest sticker, Phe is the weakest sticker, and Tyr has strengths that lie between those of Trp and Phe [13]. The measured (**Figs. 1g-i**, **ED Figs. 2b-f**) and computed (**ED Fig. 2b**) moduli show a clear dependence on sticker strengths. The presence of Phe residues increases the crossover frequency (**Fig. 1g** and **ED Figs. 2a, 2f**) and lowers the storage and loss moduli, implying that these condensates become less elastic and less viscous on all timescales. Conversely, Trp residues as stickers lower the crossover frequency and narrow the gap between the storage and loss moduli even below $\omega_{crossover}$ (**Fig. 1i** and **ED Figs. 2c-f**). These results indicate that storage moduli become higher, and $\omega_{crossover}$ is lowered as the sticker strengths are increased. Consistent with this trend, condensates formed by allY have material properties that are intermediate between those formed by allF and allW (**Fig. 1h** and **ED Fig. 2b**). Microrheology results are summarized for all A1-LCD sticker variants by plotting the loss tangent, defined as the ratio of G'' to G', as a function of frequency (**ED Fig. 2f**). Although the loss tangent does not cross 1.0 for every variant within the experimentally accessible frequency range, it is clear from the negative slope of the loss tangent at high frequencies that all A1-PLCD variants (except the allF variant) display a crossover to a predominantly elastic regime at sequence-encoded frequencies. These findings demonstrate that stronger stickers lead to higher storage moduli and increased elasticity of PLCD condensates.

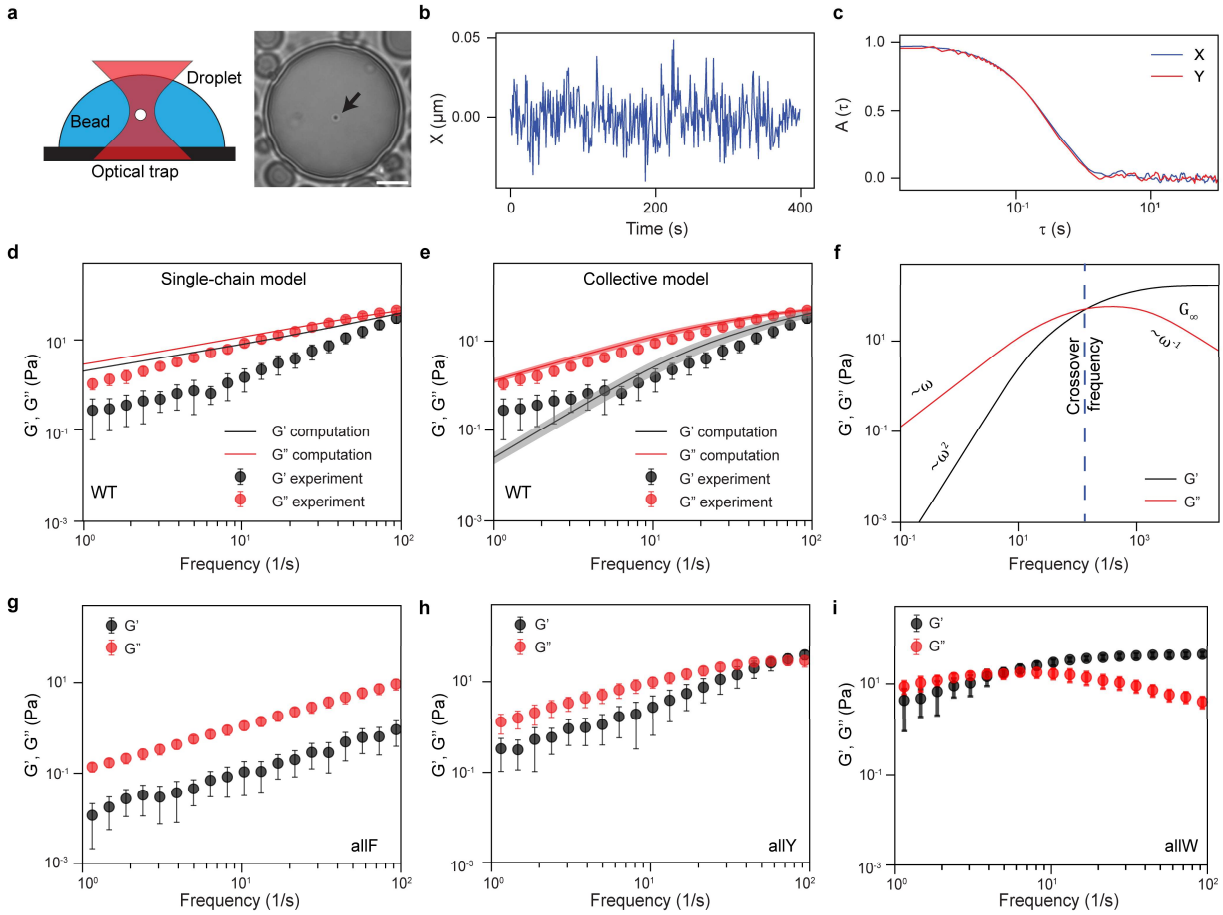

Fig. 1: PLCD condensates are viscoelastic Maxwell fluids defined by sequence-specific, frequency-dependent storage (G') and loss (G'') moduli. (a) Setup for passive microrheology with optical tweezers (left). The image on the right shows an optically-trapped 1 μm polystyrene bead within a condensate formed by WT A1-LCD. **(b)** Representative positional trajectory of a bead thermally fluctuating within the optical trap inside the condensate that is tracked along the horizontal axis. **(c)** The normalized autocorrelation function of positional fluctuations of a bead inside a condensate that is confined by the optical trap. The correlation functions measured along the horizontal and vertical axes are shown. **(d)** Dynamical moduli for WT condensates. The figure shows comparisons between measured and computed moduli, where computations use the single-chain model. (**e**) Comparisons of measured and computed moduli, as in **(d)** but using the collective model for analyzing the network structures of simulated condensates. Both measured and computed moduli show a single crossover frequency at which the dominance of the storage and loss moduli change. To put computed moduli on the same scale as experiments, we rescaled the crossover frequency for computations to match the measured value, and then compared the computed moduli to measured values across all frequencies. Error bars for measured data represent standard deviations about the mean that was computed using data for 20 condensates. The error bands for computed data are standard deviations across 10 replicates. **(f)** Dynamical moduli computed from simulations using the collective model for WT condensates. This highlights the frequency-dependent scaling of storage and loss moduli above and below the crossover frequency, which is annotated by the blue dashed line. $G' = G''$ at the crossover frequency. Note that the inverse of the frequency is the network reconfiguration time. **(g-i)** Measured dynamical moduli of condensates formed by three sequence variants: **(g)** allF, **(h)** allY, and **(i)** allW. (See Fig. ED1 for additional variants.) For **(d, e, g-i)**, symbols denote the average of G' and G''over 20 condensates. Error bars represent the standard deviation about the mean.

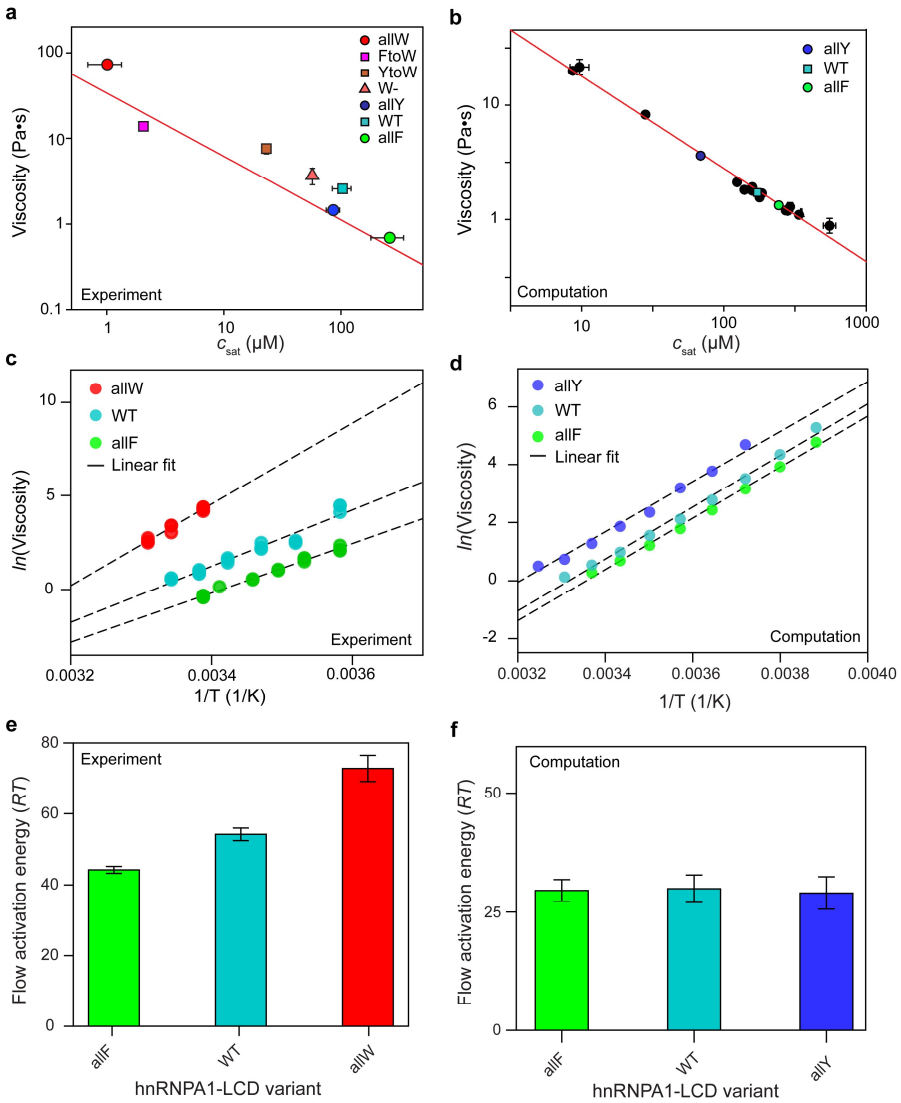

Fig. 2: Driving forces for phase separation contribute directly to viscosity of condensates and the strengths of sticker-sticker interactions determine the barriers for network reconfiguration. (a) Viscosity measured at 22 ˚C plotted against measured saturation concentrations [12] (c_{sat}) for condensates formed by WT and different A1-LCD variants. The red line is a linear fit to the double-logarithmic plot of $\log_{10}$(viscosity) versus $\log_{10}(c_{sat})$. **(b)** The viscosity computed from simulations of A1-LCD variants plotted against computed c_{sat} values at 24 ˚C. The red line shows the linear fit to the double-logarithmic plot. Variants for which experimental values also exist are highlighted with colored symbols. **(c)** Arrhenius plots of measured viscosities for condensates formed by allW, WT, and allF. **(d)** Arrhenius plots using temperature-dependent viscosities from simulations analyzed using the collective model. Data are shown for condensates of allF, WT, and allY. **(e)** Flow activation energies estimated from linear fits to the experimental data shown in **(c)**. **(f)** Flow activation energies calculated from the linear fits to the computational data shown in **(d)**. For **(e)** and **(f)** the units are in RT at the standard conditions (T = 25 ˚C), which is equivalent to 2.48 kJ/mol. For (**e**), error bars represent the error obtained from the linear fit. For (**f**), error bars are the standard deviation.

Next, we employed passive video particle tracking to measure the terminal, zero-shear viscosity at very low frequencies for nascent condensates formed by different PLCD sequences [30,31]. These viscosities are significantly higher in condensates formed by PLCD sequences with high Trp contents. The zero-shear viscosity is ~80 Pa·s for the allW variant, ~2.5 Pa·s for WT, ~1.4 Pa·s for the allY variant, and ~0.6 Pa·s for the allF variant (**Fig. 2a** and **ED Fig. 3a**). The zero-

shear viscosity becomes smaller as the driving force for phase separation is weakened. This is apparent in the plot of the logarithms of the measured viscosities and measured threshold concentrations (c_{sat}) for phase separation (**Fig. 2a**). The inverse correlation was also observed between the computed values of zero-shear viscosity and c_{sat} (**Fig. 2b**). The computations were performed for a larger number of sequence variants of A1-LCD derived from previous studies [12,13]. Using moduli derived from computations that use the collective model, we note that the crossover frequencies increase as the driving forces for phase separation are weakened (**ED Fig. 3b**). The overall inferences are that the internal viscosity of condensates and the crossover between dominantly viscous and dominantly elastic regimes are governed by the driving forces for phase separation, which are encoded by the grammars of stickers and spacers [12,13].

The strengths of intra- and intermolecular interactions within condensates will also influence the barriers to reconfiguration of condensate-spanning networks. We measured the relevant energy barriers, referred to as the flow activation energy, using thermorheology (**ED Fig. 3c**) [20,32]. To quantify the flow activation energy, we measured mean squared displacements (MSDs) of probe particles within PLCD condensates through video particle tracking as a function of temperature (**ED Fig. 3d**) and derived the temperature dependencies of viscosities of different condensates (**ED Figs. 3e, 3f**). The measured viscosities show an exponential dependence on temperature that is consistent with an Arrhenius relationship [20,33]. This relationship suggests that there is a single dominant barrier for network reconfiguration (**Fig. 2c**). The Arrhenius relationship was reproduced for viscosities derived from computations using the collective (**Fig. 2d**) and single-chain models (**ED Fig. 3g**). This indicates that the barrier to network reconfiguration is governed primarily by the ensemble of network structures that form within condensates.

From fits to the Arrhenius relationships, we extracted flow activation energies using data from measurements and computations. In units of RT, where T = 25˚C and R is the ideal gas constant, the barriers we extracted were ~30RT from computations, and these are within a factor of ~0.7 of the barriers extracted from measurements for nascent condensates formed by WT and allF (**Figs. 2e, 2f**). The computed barriers are lower than those inferred from measurements, and the mismatch can be attributed to contributions from sequence-specific internal solvation to molecular mobilities within condensates, which are not captured in the lattice-based computations. The flow activation energy for nascent condensates formed by allW is ~73 RT (**Fig. 2e**). These condensates are highly elastic, and the sticker-sticker interactions that must be broken to reconfigure the network are stronger with Trp as opposed to Phe or Tyr as stickers.

Discussions to this point highlight the contributions of stickers to the driving forces for phase separation and the direct connections between these driving forces and material properties of the dense phase. Next, we investigated the contributions of spacer residues in the context of A1-LCD. Previous studies showed that the replacement of Gly residues with Ser weakens the driving forces for phase separation [12]. This effect could be explained by the higher effective solvation volume [34] of Ser over Gly. However, even though substitutions of Gly to Ser weakened the driving forces for phase separation, simulations showed that the extents of crosslinking within condensates remained on a par with or were even higher than what was observed for condensates formed by WT and allY [13]. These observations pointed to possible separation of functions between networking and density transitions via mutations to spacers [13]. The implication is that the extent of internal crosslinking within condensates, which is governed by the associativity of multivalent macromolecules [35], does not necessarily follow the driving forces for segregative transitions such as phase separation. The latter primarily determine the free energy of transfer of molecules from

the dilute to dense phase. To test the proposal of apparent separation of function, we measured the dynamical properties of condensates formed by variants of A1-LCD where different numbers of Gly residues were replaced with Ser.

Video particle tracking measurements and computations showed that in nascent condensates formed by allY, allY^{20GtoS}, and allY^{30GtoS}, the internal viscosities decrease with weakened driving forces for phase separation (**Fig. 3a**). Condensates formed by the variant WT^{30GtoS} are highly dynamic at early time points, as seen by the motion of embedded 200 nm polystyrene particles. However, they showed evidence of dynamical arrest within a few minutes after sample preparation (**Movie S1, ED Fig. 4a**). Accordingly, we quantified the average diffusion coefficients of multiple probe particles within WT^{30GtoS} condensates as a function of time. The average diffusion coefficient decays to zero within a few minutes from the start of the experiment (**Fig. 3b**). This indicates that Gly to Ser mutations substantially accelerate the aging behavior compared to WT condensates (**ED Fig. 4b**), and this prevented quantitative measurements of viscoelastic properties of WT^{30GtoS} condensates. However, introducing Gly to Ser substitutions into the allY variant (allY^{30GtoS}) leads to a decay of the average diffusion coefficient of the probe particles to zero within ~1.5 hours of sample preparation (**Fig. 3c**). This is a slower timescale of dynamical arrest when compared to condensates formed by WT^{30GtoS}. We were able to tune the timescales for the onset of dynamical arrest by titrating the Gly to Ser substitutions. This is shown in root mean squared displacement (RMSD) histograms collected from particle tracking measurements of more than 10^3 probe particles within different condensates during the first hour (0 hrs) and at later times after sample preparation (3 hrs or 24 hrs) (**Fig. 3d, top, middle,** and **bottom**). In the absence of spacer mutations, the ensemble-averaged MSDs of probe particles within allY condensates did not show any significant alterations even after 24 hrs (**Fig. 3e**). In contrast, the MSD measurements showed time-dependent dynamics for condensates formed by the allY^{20GtoS} and allY^{30GtoS} variants (**ED Fig. 4c,** and **Fig. 3f**). At early time points (0 hrs), the particles within allY^{30GtoS} condensates showed diffusive behavior as expected for a material that behaves as a viscous fluid at long timescales. However, after 3 hrs, the observed MSD curves were sublinear (**Fig. 3f**), indicating sub-diffusive motion of the probe particles. The flatness of the MSD curves at longer lag-times indicates that the translational diffusion of probe particles becomes caged due to the onset of stable elastic networks [36] in condensates formed by allY^{30GtoS}. Indeed, the histogram of RMSDs, which initially showed a peak around an RMSD of ~0.25 μm, showed a sharp peak near zero within 3 hours, indicating complete dynamical arrest of the condensate (**Fig. 3d, bottom**).

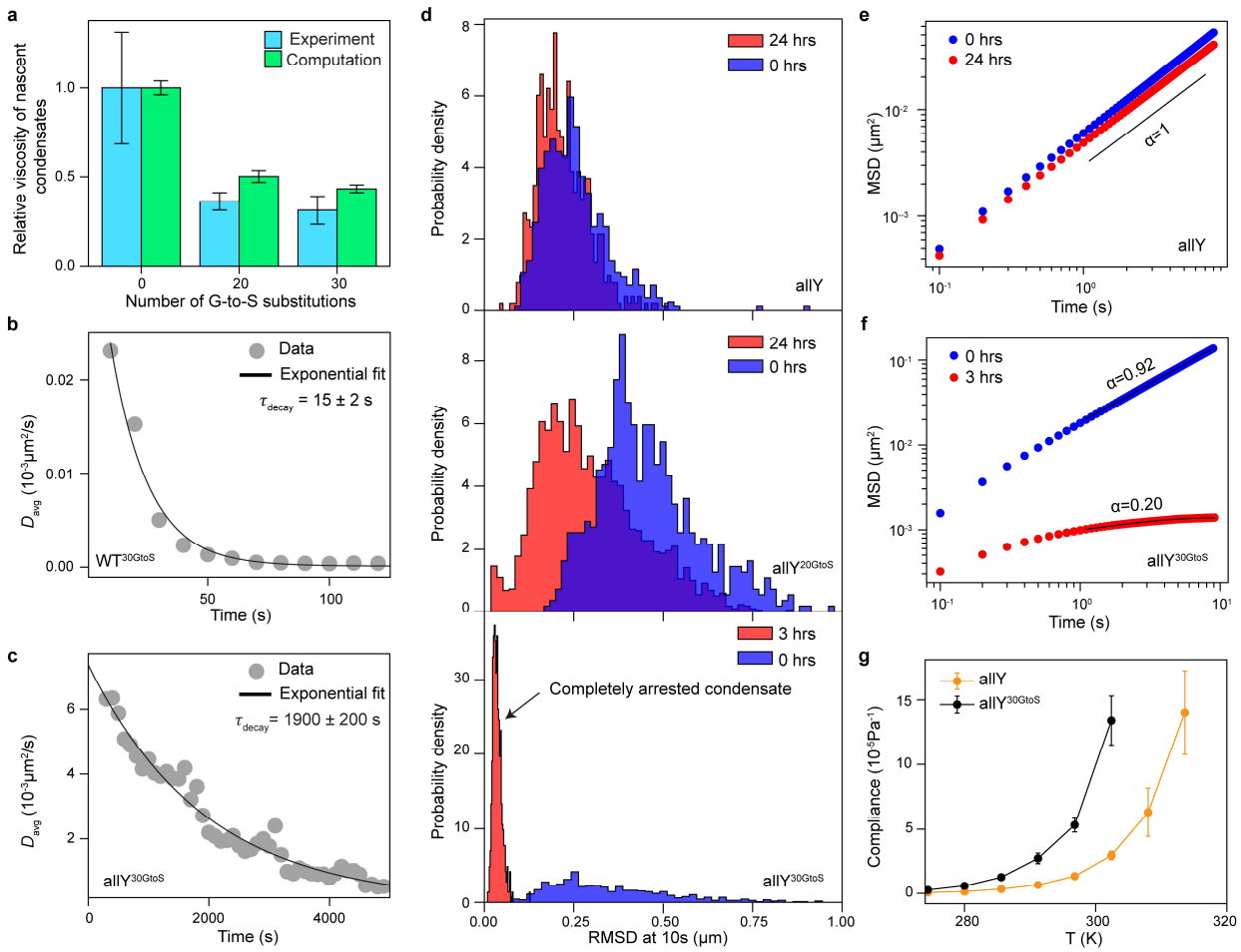

Fig. 3: Mutations that alter spacers of A1-LCD accelerate the dynamical arrest of condensates. (a) Relative changes in viscosities within nascent condensates, calibrated against the allY system, and quantified as a function of different numbers of Gly to Ser substitutions. Data are shown for relative viscosities from measurements and computations, where the latter uses the collective model for the Zimm matrix. Error bars represent the standard deviation in the estimate of the mean relative viscosity. Experimental viscosities are obtained from at least 5 experiments featuring at least 50 tracked particles in each measurement. **(b)** Average diffusion coefficient of 200 nm polystyrene beads within WT^{30GtoS} condensates measured as a function of time following the start of sample imaging. The black line shows an exponential decay fit with the characteristic decay times τ_{decay} as indicated. **(c)** same as **(b)** but for $allY^{30GtoS}$ condensates. **(d)** Histograms for the Root Mean Squared Displacement (RMSD) of 200 nm polystyrene beads measured at 10 s lag times within nascent and aged condensates. The top, middle, and bottom panels show histograms for nascent (blue) and aged (red) condensates (ages of condensates are in the legends) formed by allY, $allY^{20GtoS}$, $allY^{30GtoS}$, respectively. **(e)** Ensemble-averaged MSD of 200 nm beads in nascent (blue) or aged (red) allY condensates. **(f)** Same as **(e)** but for $allY^{30GtoS}$ condensates. **(g)** Temperature-dependent compliance computed from the simulations for condensates formed by allY and $allY^{30GtoS}$. We use the collective model for computing the Zimm matrix. Error bars are standard deviations of the mean compliance values computed using three replicates.

Taken together, the picture that emerges from alterations to the WT spacers is as follows: Gly to Ser substitutions on a common allY background of stickers weaken the driving forces for condensate formation. Viscosities of nascent condensates are lowered with the increased number of Gly to Ser substitutions. Despite these seemingly intuitive observations, we also find unexpected behaviors such as the onset of dynamical arrest and accelerated physical aging of the dense phase

due to Gly to Ser substitutions. Importantly, the timescales for complete dynamical arrest decrease with increasing numbers of Gly to Ser substitutions (**Fig. 3d**).

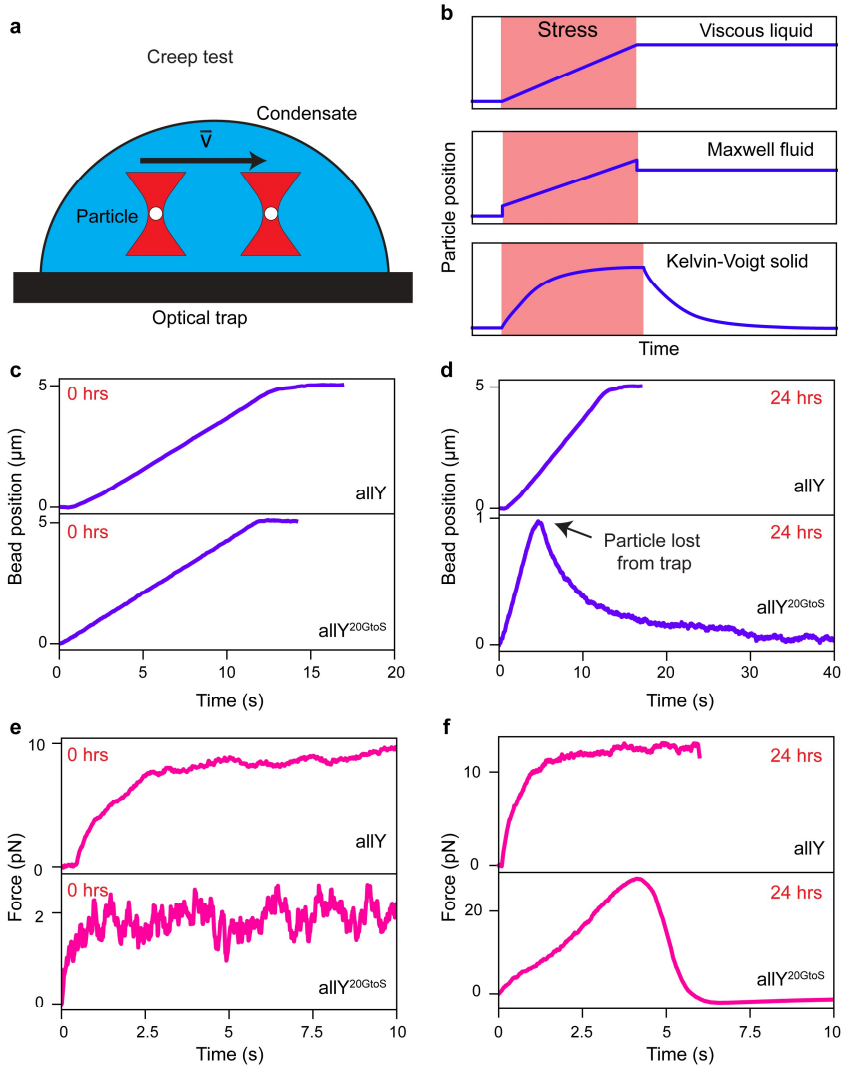

Fig. 4: Dynamically arrested PLCD condensates resemble Kelvin-Voigt solids with terminally elastic behavior. **(a)** Schematic of the optical tweezer-based creep test microrheology experiment. A bead is trapped within a condensate using an optical trap. The trap is programmed to move a set distance (here 5 μm) at a constant velocity (0.5 μm/s). The bead position and the force exerted by the condensate on the bead are monitored via a camera and a quadrant photodetector, respectively. **(b)** Expected bead position in response to the trap movement during the creep test for a viscous liquid, a viscoelastic Maxwell fluid, and a Kelvin-Voigt solid. **(c)** Bead position as a function of time in response to the programmed trap movement in nascent allY and allY^{30GtoS} condensates. **(d)** Same as (**c**) but for aged allY and aged allY^{20GtoS} condensates (24 hrs). Note that the bead in allY^{20GtoS} condensate recoils back to its initial position after ~1 μm travel, indicating that the condensate is exerting an elastic force that overpowers the force exerted by the optical trap. As shown in panel **(b)**, this response is characteristic of a viscoelastic solid. **(e)** Force exerted on the bead by the condensate network during the creep test experiment. Data are shown for freshly prepared allY and allY^{20GtoS} condensates. The saturation of the force is a characteristic of the viscous drag force, which depends on the velocity of the trap, the viscosity of the condensate, and the size of the bead. **(f)** Same as **(e)** but for aged condensates. The data in the bottom of panel **(f)** indicate that aged condensates formed by allY^{20GtoS} behave like Kelvin-Voigt solids.

Comparison with the top panel highlights the fact that these condensates transition from being Maxwell fluids at early time points to elastic, Kelvin-Voigt solids as they age.

What may the molecular origins be of accelerated dynamical arrest caused by Gly to Ser substitutions? Increasing the number of Gly to Ser substitutions increases the compliance of networks formed within nascent condensates (**Fig. 3g**). This was inferred from simulation results, which only capture the properties of nascent condensates. The zero-shear compliance quantifies the maximal network reconfiguration achievable at a given stress. Across all temperatures, the compliance was found to be systematically higher for variants with increased numbers of Gly to Ser substitutions (**Fig. 3g**). Increased compliance should enable facile network rearrangements and the question is if these rearrangements enable fundamental changes to material properties of condensates as they physically age.

To investigate the dynamical transitions that accompany condensate aging upon mutations of spacer residues, we employed active microrheology using an optical tweezer-based creep test [37] (**Fig. 4a** and **ED Fig. 5a**). In the creep test, a polystyrene particle is trapped within the condensate and dragged across at a constant velocity (**Fig. 4a**). This ensures a constant strain rate within the condensate. We recorded how the particle followed the traveling optical trap, and simultaneously measured the forces exerted on the particle by the internal networks of condensates. The expected response of a material with terminally viscous behavior is that the particle will follow the trap until the optical trap is stopped [38] (**Fig. 4b, top** and **ED Fig. 5a, bottom**). For a Maxwell fluid, the bead will also follow the trap but with a lag time that is governed by the terminal relaxation time of the fluid [38] (**Fig. 4b, middle** and **ED Fig. 5a, middle**). Finally, for a Kelvin-Voigt viscoelastic solid, the particle will follow the trap to a certain extent before recoiling to its initial position [38] (**Fig. 4b, bottom** and **ED Fig. 5a, top**). This is because a Kelvin-Voigt material is terminally elastic. Hence, it allows local motions of the particle at short timescales whereas at longer timescales, the particle is constrained within physical cages that are setup by elastic networks that form on system-specific length scales [39].

We performed optical tweezer-based creep tests on allY and allY^{20GtoS} condensates. At 0 hrs, both condensates showed terminally viscous fluid behavior where the bead traveled along with the optical trap for the entire traveling distance of 5 μm (**Fig. 4c**). At 24 hrs, the allY condensates still displayed a terminally viscous behavior (**Movie S2, Fig. 4d, top**). However, the allY^{20GtoS} condensates exhibited behaviors consistent with viscoelastic solids (**Movie S3, Fig. 4d, bottom**). Specifically, the probe particle was lost from the optical trap at ~1 μm. Upon being lost from the trap, the probe particle slowly recoiled back to its original position. We simultaneously measured the forces exerted on the probe particle by condensate networks during creep test experiments. In nascent allY and allY^{20GtoS} condensates, the saturation of the force is a characteristic of the viscous drag force [40], which depends on the velocity of the trap, and the viscosity of the condensate, but is independent of the distance (**Fig. 4e, top**). However, while this behavior is preserved for the allY condensates investigated 24 hrs after sample preparation (**Fig. 4e, bottom**), the profile is very different for the aged condensates formed by allY^{20GtoS} (**Fig. 4f, top** versus **bottom**). We systematically increased the stiffness of the trap by increasing the trapping power and observed that the maximum displacements traversed (**ED Figs. 5b, 5c**) and the force traces for the bead within allY condensates do not show changes over 24 hours (**ED Figs. 5f, 5g**). In contrast, the maximum distance traveled as well as the maximum force experienced by the particle increased for allY^{20GtoS} condensates over time (**ED Figs. 5d, 5h, 5e, 5i**). This indicates that the restoring force responsible for the particle recoil in aged allY^{20GtoS} condensates is elastic.

Next, we asked if dynamical arrest induces changes to the morphologies of condensates, which we investigated using differential interference contrast (DIC) microscopy (**Fig. 5a**). Surprisingly, despite showing a definitive transition from a Maxwell fluid to a Kelvin-Voigt solid (**Figs. 4d, 4f**), the micron-scale morphologies of nascent versus aged condensates formed by allY^{20GtoS} remain essentially the same (**Fig. 5a**). Previous studies showed that liquid-to-solid transitions can be accompanied by the formation of amyloid fibrils [41,42]. To test for this possibility, we stained aged condensates formed by different sequence variants of A1-LCD using the amyloid-sensitive dye Thioflavin T (ThT). While this dye shows positive staining for fibrils formed by the microtubule-binding protein Tau after 24 hrs, it does not show positive staining for any of the aged PLCD condensates studied in this work (**Fig. 5b**). We conclude that the fluid-to-solid transitions observed for condensates formed by variants such as allY^{20GtoS} result in the formation of non-fibrillar, elastic solids.

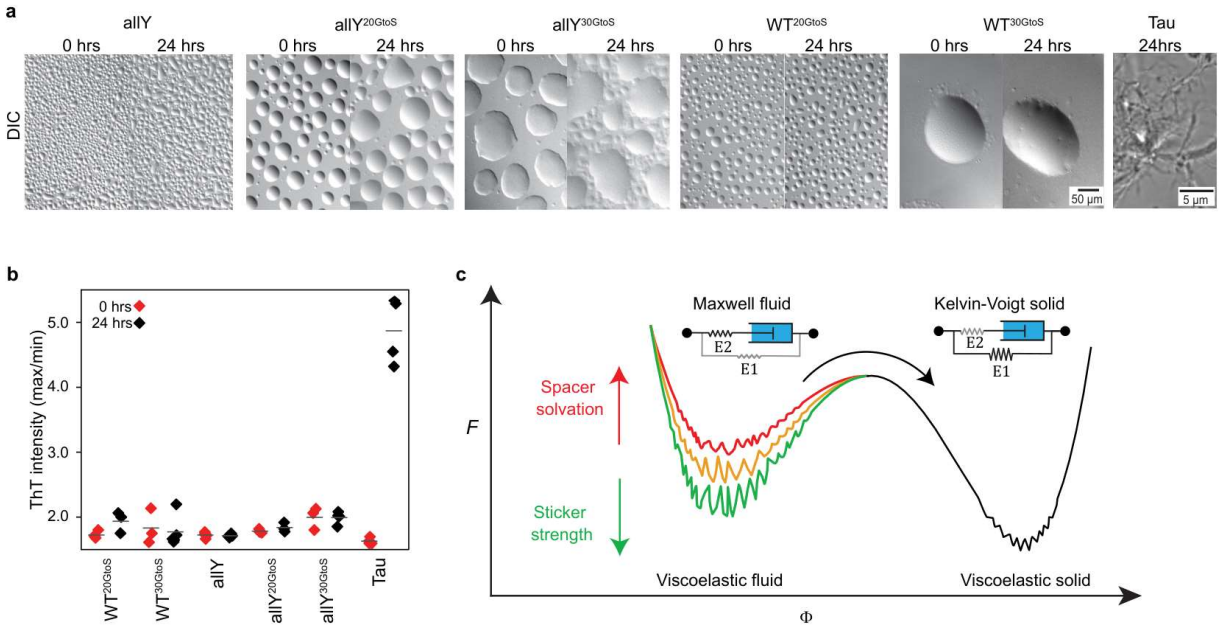

Fig. 5: Aged condensates are non-fibrillar solids implying that aging is accompanied by transitions from metastable, terminally viscous fluids to stable, terminally elastic solids. (a) Representative images from DIC microscopy of different condensates at 0 hrs and after 24 hrs from sample preparation. Tau fibrils are shown for comparison. **(b)** ThT fluorescence ratios of the maximal / minimal intensities for freshly prepared condensates and 24 hrs old condensates for various A1-LCD variants. No changes were observed in ThT staining for condensates formed as a function of aging. As a positive control, we show data for amyloid fibrils formed by the protein Tau after 24 hrs from sample preparation. The horizontal line represents the mean ThT fluorescence over four different sample preparations. (c) Proposed free energy profiles $F(\Phi)$, which we write as a sum of a Landau free energy [43] and a Zwanzig rough potential [44]. The order parameter $0 \leq \Phi \leq 1$ quantifies the extent of crosslinking, which controls the rigidity and elasticity of the material. Free energy landscapes of dense phases suggest that evolved molecular grammars code for PLCD condensates being long-lived metastable fluids even if globally minima are elastic solids. Distinct free energy profiles are intended to represent variants with increased numbers of Gly to Ser substitutions (cool to hot colors). It appears that weakening of the driving forces for forming condensates that are terminally viscous fluids leads to a lowering of the barrier for conversion to terminally elastic solids. This separation of functions is evident from the fact that while c_{sat} for forming terminally viscous condensates increases with mutations to spacers, the extent of intra-condensate crosslinking remains unchanged for these variants [13]. However, the networks become more compliant, and this is likely to facilitate facile rearrangements that drive the conversion from terminally viscous fluids to elastic solids.

Recently, Jawerth et al. used microrheology to characterize condensates formed by the protein PGL3 [19]. They found that nascent condensates formed by this protein are Maxwell fluids. They also found that aged condensates continue to behave as Maxwell fluids, even though the condensates no longer fused, and rheology measurements suggested that the aged condensates were dynamically arrested. Based on their observations, Jawerth et al. proposed that the PGL3 condensates were "Maxwell glasses" defined as Maxwell fluids showing age-dependent terminal relaxation times [19]. Their findings suggest that, irrespective of their physical age, the rheological properties of condensates will always conform to that of a Maxwell fluid.

In contrast to the report of Jawerth et al.,[19] we find that dynamical arrest is congruent with a clear and measurable transition between a Maxwell fluid and a Kelvin-Voigt solid. Therefore, for PLCD condensates, the dynamically arrested state that emerges upon physical aging is a terminally elastic solid. Based on these observations, we propose that the phase behaviors of PLCDs are best described using a bistable model whereby the free energies of dense phases are written in terms of an order parameter Φ that represents the extent of physical crosslinking between molecules within condensates (**Fig. 5c**). The material state with the highest degree of non-random crosslinking [13] will be the global free energy minimum. In this scenario, viscoelastic fluids, defined by dominant elastic behaviors at short timescales and terminally viscous behaviors, will be metastable. On average, the value of Φ will be small and closer to zero for metastable fluid-like states. Fluid-to-solid transitions appear to be continuous phase transitions[43] whereby the viscoelastic solid phase appears continuously from a metastable Maxwell fluid phase. This proposal is congruent with observations where we find an exponential scaling of bead diffusion coefficients as the condensates age (**Figs. 3b, 3c**). Our current data are consistent with the metastability of fluid states being enhanced by increased sticker strengths and weakened by mutations to spacers (**Fig. 5c**).

The free energy profiles in **Fig. 5c** are annotated by two additional features. The terminally fluid and solid phases are represented using a standard linear solid or Zener model [45]. In this model, a time-dependent rise of the elasticity of the E1 element captures the transitions from a dominant Maxwell-type behavior of nascent condensates ($E1 < E_2$) to a Kelvin-Voigt-type behavior as condensates age ($E1 >> E_2$). We also allow for the possibility that increased metastability of the fluid state arises from ruggedness within the well that corresponds to low values of Φ. Our proposal represents a combination of the Landau picture [43] of continuous transitions along Φ and the Zwanzig picture [44] of roughness within a well. Inclusion of the latter comes from its invocation as an explanation for slow coarsening of fluid-like condensates [46] where the viscous fluid is presumed to be the terminal state of nascent as well as aged condensates.

Recent bioinformatics analyses showed an inverse correlation between sticker and spacer identities [12]. Increasing the number of Tyr stickers is positively correlated with increased numbers of Gly residues as spacers. In contrast, increased numbers of Phe stickers are accompanied by increased number of Ser residues as spacers. In cellular measurements of PLCDs that form solids, there is a preference for high numbers of Phe stickers and Ser residues as spacers [47]. Finally, Trp is used sparingly as a sticker in PLCDs [12,14]. Taken together, these trends suggest an evolutionarily encodable preference whereby certain PLCDs form condensates that are metastable Maxwell fluids. How this plays out for condensates formed by mixtures of PLCDs with compositionally distinct preferences will need further investigation. Importantly, being able to compute moduli from simulations of the network structures of condensates [13] will allow us to design PLCD

sequences with bespoke material properties [48]. This will also enable direct interrogations of how material properties affect condensate functions *in vitro* and *in vivo*.

Previous work showed that the linear patterning of aromatic stickers affects the formation of fluid- versus solid-like condensates [11,49]. Wang et al., showed that mutations to spacers can have a direct impact on the time-dependent changes to biomolecular mobility in the dense phase probed by fluorescence recovery after photobleaching [50]. Given the large barriers we estimate for network rearrangements (**Fig. 2e, f**), it appears that for many naturally occurring systems, including PLCDs, the barrier to conversion from terminally viscous fluids to terminally elastic solids might be insurmountable on biologically relevant timescales. This might explain the growing accounts invoking "dynamicity" [4,6,7] as a key attribute for functions of condensates, with a few key exceptions [49].

Acknowledgments

This work was supported by the US National Institutes of Health through grant R01NS121114 (T.M. and R.V.P), and the St. Jude Children's Research Collaborative on the Biology and Biophysics of RNP granules (P.R.B., T.M., and R.V.P). P.R.B. acknowledges support by the National Institute of General Medical Sciences (NIGMS) of the National Institutes of Health (R35 GM138186). S.R.C. acknowledges support by the National Institutes of Health (T32 EB028092). We acknowledge T. Mahendran for help with Tau protein purifications and with the ThT assay of Tau amyloid fibers. We thank George Campbell from the Cell and Tissue Imaging Center at St. Jude CRH for his assistance with light microscopy.

Author contributions

Conceptualization: P.R.B., R.V.P., and T.M.; Methodology: P.R.B., I.A., W.M.B., S.R.C., R.V.P., and T.M.; Investigation: I.A., W.M.B., S.R.C., M.F., A.S., A.B., P.R.B., R.V.P., and T.M.; Resources: P.R.B., R.V.P., and T.M.; Writing – original draft: P.R.B., R.V.P., and T.M.; Writing – reviewing and editing: all authors; Funding acquisition: P.R.B., R.V.P., and T.M.

Competing interests

All authors declare no competing interests.

Data and materials availability

All data are available in the manuscript or the supplementary materials. All expression plasmids are available from T.M. under a material transfer agreement with St. Jude Children's Hospital. Codes for microrheology data analysis are available on GitHub (see https://github.com/BanerjeeLab-repertoire/Material-properties). All simulation results are accessible via: https://github.com/Pappulab/PLCD-Data-Repository-and-Analysis-Routines and the code for computation of moduli are available via the Pappu Lab Github https://github.com/Pappulab.

References

1 Berry, J., Brangwynne, C. P. & Haataja, M. Physical principles of intracellular organization via active and passive phase transitions. *Reports on Progress in Physics* **81**, 046601, doi:10.1088/1361-6633/aaa61e (2018).

2 Mittag, T. & Pappu, R. V. A conceptual framework for understanding phase separation and addressing open questions and challenges. *Molecular Cell* (2022).

3 Banani, S. F., Lee, H. O., Hyman, A. A. & Rosen, M. K. Biomolecular condensates: organizers of cellular biochemistry. *Nature Reviews in Molecular and Cell Biology* **18**, 285-298, doi:10.1038/nrm.2017.7 (2017).

4 Alberti, S. & Hyman, A. A. Biomolecular condensates at the nexus of cellular stress, protein aggregation disease and ageing. *Nature Reviews Molecular Cell Biology* **22**, 196-213, doi:10.1038/s41580-020-00326-6 (2021).

5 Putnam, A., Cassani, M., Smith, J. & Seydoux, G. A gel phase promotes condensation of liquid P granules in Caenorhabditis elegans embryos. *Nature Structural & Molecular Biology* **26**, 220-226, doi:10.1038/s41594-019-0193-2 (2019).

6 Li, W. *et al.* Biophysical properties of AKAP95 protein condensates regulate splicing and tumorigenesis. *Nature cell biology* **22**, 960-972 (2020).

7 Shi, B. *et al.* UTX condensation underlies its tumour-suppressive activity. *Nature* **597**, 726-731, doi:10.1038/s41586-021-03903-7 (2021).

8 Lafontaine, D. L. J., Riback, J. A., Bascetin, R. & Brangwynne, C. P. The nucleolus as a multiphase liquid condensate. *Nature Reviews in Molecular and Cell Biology* **22**, 165-182, doi:10.1038/s41580-020-0272-6 (2021).

9 Mathieu, C., Pappu, R. V. & Taylor, J. P. Beyond aggregation: Pathological phase transitions in neurodegenerative disease. *Science* **370**, 56-60, doi:doi:10.1126/science.abb8032 (2020).

10 Yu, H. *et al.* HSP70 chaperones RNA-free TDP-43 into anisotropic intranuclear liquid spherical shells. *Science* **371**, eabb4309, doi:doi:10.1126/science.abb4309 (2021).

11 Martin, E. W. *et al.* Valence and patterning of aromatic residues determine the phase behavior of prion-like domains. *Science* **367**, 694-699 (2020).

12 Bremer, A. *et al.* Deciphering how naturally occurring sequence features impact the phase behaviours of disordered prion-like domains. *Nature Chemistry* **14**, 196-207, doi:10.1038/s41557-021-00840-w (2022).

13 Farag, M. *et al.* Condensates formed by prion-like low-complexity domains have small-world network structures and interfaces defined by expanded conformations. *Nature Communications* **13**, 1-15 (2022).

14 Farag, M., Borcherds, W. M., Bremer, A., Mittag, T. & Pappu, R. V. Phase Separation in Mixtures of Prion-Like Low Complexity Domains is Driven by the Interplay of Homotypic and Heterotypic Interactions. *bioRxiv*, 2023.2003.2015.532828, doi:10.1101/2023.03.15.532828 (2023).

15 Boulay, G. *et al.* Cancer-Specific Retargeting of BAF Complexes by a Prion-like Domain. *Cell* **171**, 163-178 e119, doi:10.1016/j.cell.2017.07.036 (2017).

16 Davis, R. B., Kaur, T., Moosa, M. M. & Banerjee, P. R. FUS oncofusion protein condensates recruit mSWI/SNF chromatin remodeler via heterotypic interactions between prion-like domains. *Protein Science* **30**, 1454-1466, doi:https://doi.org/10.1002/pro.4127 (2021).

17 Choi, J.-M., Holehouse, A. S. & Pappu, R. V. Physical principles underlying the complex biology of intracellular phase transitions. *Annual Review of Biophysics* **49** (2020).

18 Wu, T., King, M. R., Farag, M., Pappu, R. V. & Lew, M. D. Single fluorogen imaging reveals spatial inhomogeneities within biomolecular condensates. *bioRxiv*, 2023.2001.2026.525727, doi:10.1101/2023.01.26.525727 (2023).

19 Jawerth, L. *et al.* Protein condensates as aging Maxwell fluids. *Science* **370**, 1317-1323 (2020).

20 Alshareedah, I., Singh, A., Quinn, A. & Banerjee, P. R. Determinants of Viscoelasticity and Flow Activation Energy in Biomolecular Condensates. *bioRxiv*, https://doi.org/10.1101/2022.1112.1130.522262 (2022).

21 Ghosh, A., Kota, D. & Zhou, H.-X. Shear relaxation governs fusion dynamics of biomolecular condensates. *Nature Communications* **12**, 5995, doi:10.1038/s41467-021-26274-z (2021).

22 Alshareedah, I., Moosa, M. M., Pham, M., Potoyan, D. A. & Banerjee, P. R. Programmable viscoelasticity in protein-RNA condensates with disordered sticker-spacer polypeptides. *Nat Commun* **12**, 6620, doi:10.1038/s41467-021-26733-7 (2021).

23 Bergeron-Sandoval, L. P. *et al.* Endocytic proteins with prion-like domains form viscoelastic condensates that enable membrane remodeling. *Proceedings of the National Academy of Sciences* **118**, e2113789118, doi:10.1073/pnas.2113789118 (2021).

24 Choi, J.-M., Dar, F. & Pappu, R. V. LASSI: A lattice model for simulating phase transitions of multivalent proteins. *PLOS Computational Biology* **15**, e1007028, doi:10.1371/journal.pcbi.1007028 (2019).

25 Eichinger, B. E. Configuration Statistics of Gaussian Molecules. *Macromolecules* **13**, 1-11, doi:10.1021/ma60073a001 (1980).

26 Yang, Y. & Yu, T. Graph theory of viscoelasticities for polymers with starshaped, multiple-ring and cyclic multiple-ring molecules. *Die Makromolekulare Chemie* **186**, 609-631, doi:https://doi.org/10.1002/macp.1985.021860315 (1985).

27 Rouse, P. E. A Theory of the Linear Viscoelastic Properties of Dilute Solutions of Coiling Polymers. *Journal of Chemical Physics* **21**, 1272-1280, doi:Doi 10.1063/1.1699180 (1953).

28 Zimm, B. H. Dynamics of Polymer Molecules in Dilute Solution: Viscoelasticity, Flow Birefringence and Dielectric Loss. *The Journal of Chemical Physics* **24**, 269-278, doi:10.1063/1.1742462 (1956).

29 Newman, M. *Networks: An Introduction*. (Oxford University Press, 2010).

30 Alshareedah, I., Kaur, T. & Banerjee, P. R. in *Methods in Enzymology* (Academic Press, 2020).

31 Alshareedah, I., Thurston, G. M. & Banerjee, P. R. Quantifying viscosity and surface tension of multicomponent protein-nucleic acid condensates. *Biophys J* **120**, 1161-1169, doi:10.1016/j.bpj.2021.01.005 (2021).

32 Schlenoff, J. B. & Akkaoui, K. Dissecting dynamics near the glass transition using polyelectrolyte complexes. *Macromolecules* **54**, 3413-3422 (2021).

33 Messaâdi, A. *et al.* A New Equation Relating the Viscosity Arrhenius Temperature and the Activation Energy for Some Newtonian Classical Solvents. *Journal of Chemistry* **2015**, 163262, doi:10.1155/2015/163262 (2015).

34 Harmon, T. S., Holehouse, A. S., Rosen, M. K. & Pappu, R. V. Intrinsically disordered linkers determine the interplay between phase separation and gelation in multivalent proteins. *eLife* **6**, 30294, doi:10.7554/eLife.30294 (2017).

35 Pappu, R. V., Cohen, S. R., Dar, F., Farag, M. & Kar, M. Phase Transitions of Associative Biomacromolecules. *Chemical Reviews*, doi:10.1021/acs.chemrev.2c00814 (2023).

36 Steigmann, D. J. & Pipkin, A. C. Equilibrium of elastic nets. *Philosophical Transactions of the Royal Society of London. Series A: Physical and Engineering Sciences* **335**, 419-454, doi:doi:10.1098/rsta.1991.0056 (1991).

37 Robertson-Anderson, R. M. Optical Tweezers Microrheology: From the Basics to Advanced Techniques and Applications. *ACS Macro Letters* **7**, 968-975, doi:10.1021/acsmacrolett.8b00498 (2018).

38 Roeder, R. K. Mechanical characterization of biomaterials. *Characterization of biomaterials*, 49-104 (2013).

39 Greinert, N., Wood, T. & Bartlett, P. Measurement of effective temperatures in an aging colloidal glass. *Phys Rev Lett* **97**, 265702, doi:10.1103/PhysRevLett.97.265702 (2006).

40 Hu, J. L. *et al.* Size- and speed-dependent mechanical behavior in living mammalian cytoplasm. *P Natl Acad Sci USA* **114**, 9529-9534, doi:10.1073/pnas.1702488114 (2017).

41 Patel, A. *et al.* A liquid-to-solid phase transition of the ALS protein FUS accelerated by disease mutation. *Cell* **162**, 1066-1077 (2015).

42 Molliex, A. *et al.* Phase separation by low complexity domains promotes stress granule assembly and drives pathological fibrillization. *Cell* **163**, 123-133 (2015).

43 Landau, L. The Theory of Phase Transitions. *Nature* **138**, 840-841, doi:10.1038/138840a0 (1936).

44 Zwanzig, R. Diffusion in a rough potential. *Proceedings of the National Academy of Sciences* **85**, 2029-2030, doi:doi:10.1073/pnas.85.7.2029 (1988).

45 Xiao, R., Sun, H. & Chen, W. An equivalence between generalized Maxwell model and fractional Zener model. *Mechanics of Materials* **100**, 148-153, doi:https://doi.org/10.1016/j.mechmat.2016.06.016 (2016).

46 Lee, C. F. Scaling law and universal drop size distribution of coarsening in conversion-limited phase separation. *Physical Review Research* **3**, 043081, doi:10.1103/PhysRevResearch.3.043081 (2021).

47 Posey, A. E. *et al.* Mechanistic Inferences From Analysis of Measurements of Protein Phase Transitions in Live Cells. *Journal of Molecular Biology* **433**, 166848, doi:https://doi.org/10.1016/j.jmb.2021.166848 (2021).

48 Dai, Y. *et al.* Programmable synthetic biomolecular condensates for cellular control. *Nature Chemical Biology* **19**, 518-528, doi:10.1038/s41589-022-01252-8 (2023).

49 Holehouse, A. S., Ginell, G. M., Griffith, D. & Böke, E. Clustering of Aromatic Residues in Prion-like Domains Can Tune the Formation, State, and Organization of Biomolecular Condensates. *Biochemistry* **60**, 3566-3581, doi:10.1021/acs.biochem.1c00465 (2021).

50 Wang, J. *et al.* A molecular grammar governing the driving forces for phase separation of prion-like RNA binding proteins. *Cell* **174**, 688-699. e616 (2018).

Extended Data

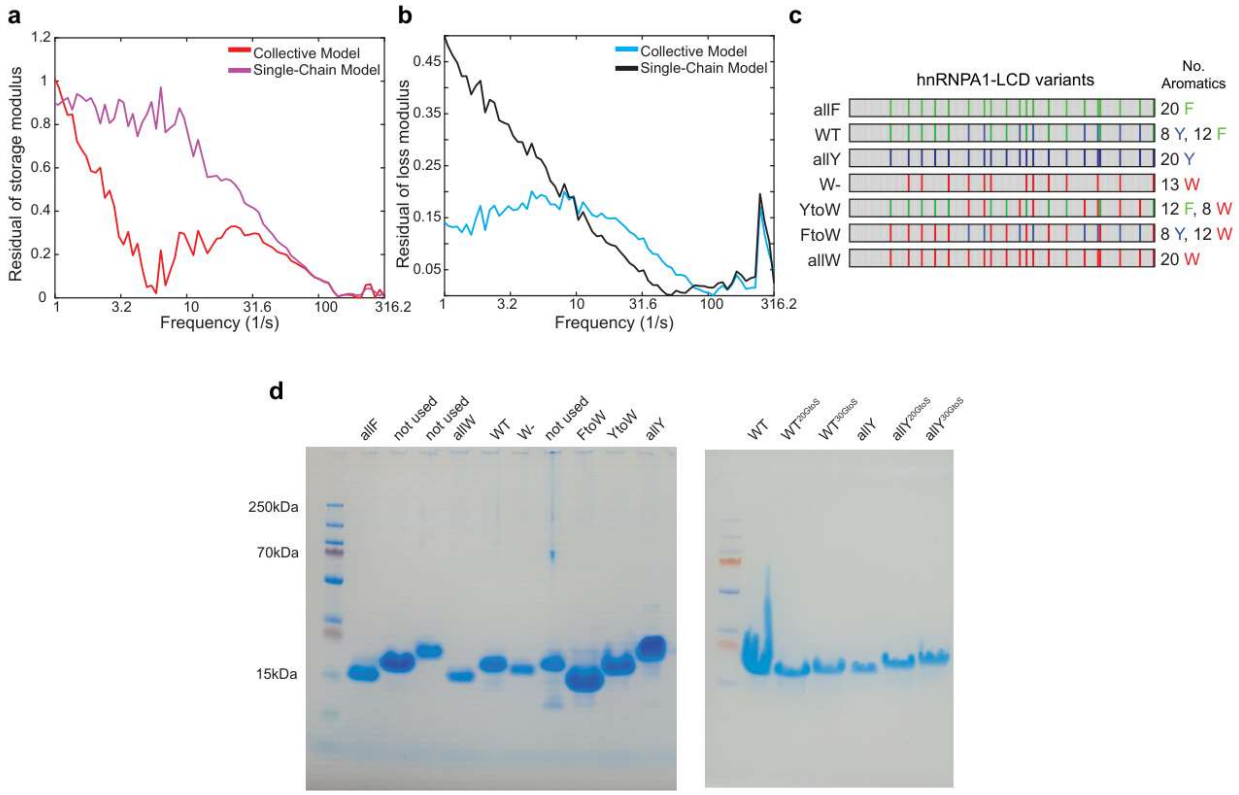

ED Fig. 1. (a) Residuals for condensates formed by WT A1 LCD between computed storage modulus using the single-chain (magenta) and collective models (red) referenced to the measured storage modulus. The residuals were computed as the absolute values of differences between the logarithms of the computed and measured moduli. Values of zero imply exact matches, values of one imply a discrepancy of an order of magnitude, and so on. At low frequencies, the sharp increase in residuals for the collective model is partly due to increased noise in the experimentally derived storage moduli. **(b)** Residuals between computed loss modulus using the single-chain (black) or collective chain dynamics (blue) and measured loss modulus for WT. The residuals were computed as in panel (**a**). **(c)** A schematic diagram of the constructs deployed in the various measurements summarized in this work. Grey represents non-aromatic spacer residues, whereas colored stripes represent the locations of the indicated aromatic residues. (**d**) SDS-PAGE gel image of purified proteins used for the experiments.

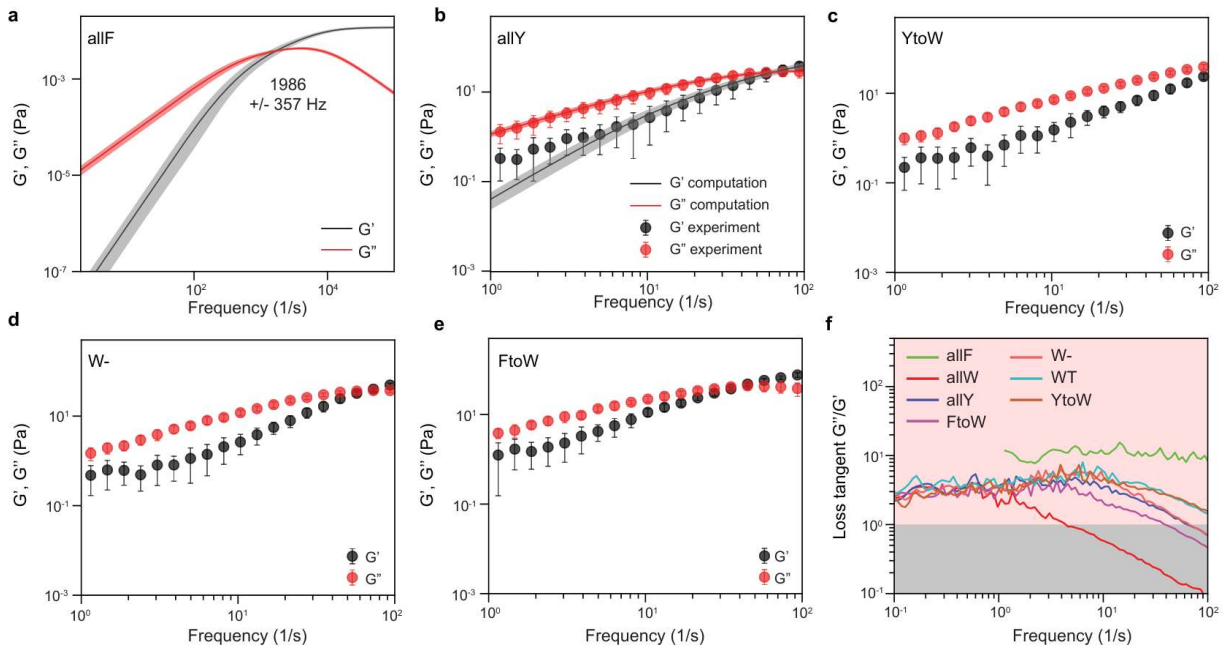

ED Fig. 2. (a) Computed dynamical moduli for condensates formed by allF. Analysis of the simulation results was performed using the collective model. This variant, as with all other variants, forms nascent condensates that are Maxwell fluids. The crossover frequency is indicated in the legend. The error band for the computed data represents the standard deviation from 3 replicates. **(b)** Measured dynamical moduli (symbols) for condensates formed by allY. Error bars represent the standard deviation as calculated from the moduli of 20 condensates. Also plotted are the computed moduli based on the analysis of simulation results using the collective model (lines). Error bands are calculated as in (**a**). **(c)-(e)** Measured dynamical moduli for condensates formed by **(c)** YtoW, **(g)** W-, and **(e)** FtoW variants of A1 LCD. Error bars are standard deviations as calculated from the moduli of 20 condensates. **(f)** Loss tangents for different variants and plotted against frequency. The loss tangents are calculated from measured moduli. The shaded regions are color coded as follows: *red* indicates dominantly viscous behavior; *grey* indicates dominantly elastic behavior.

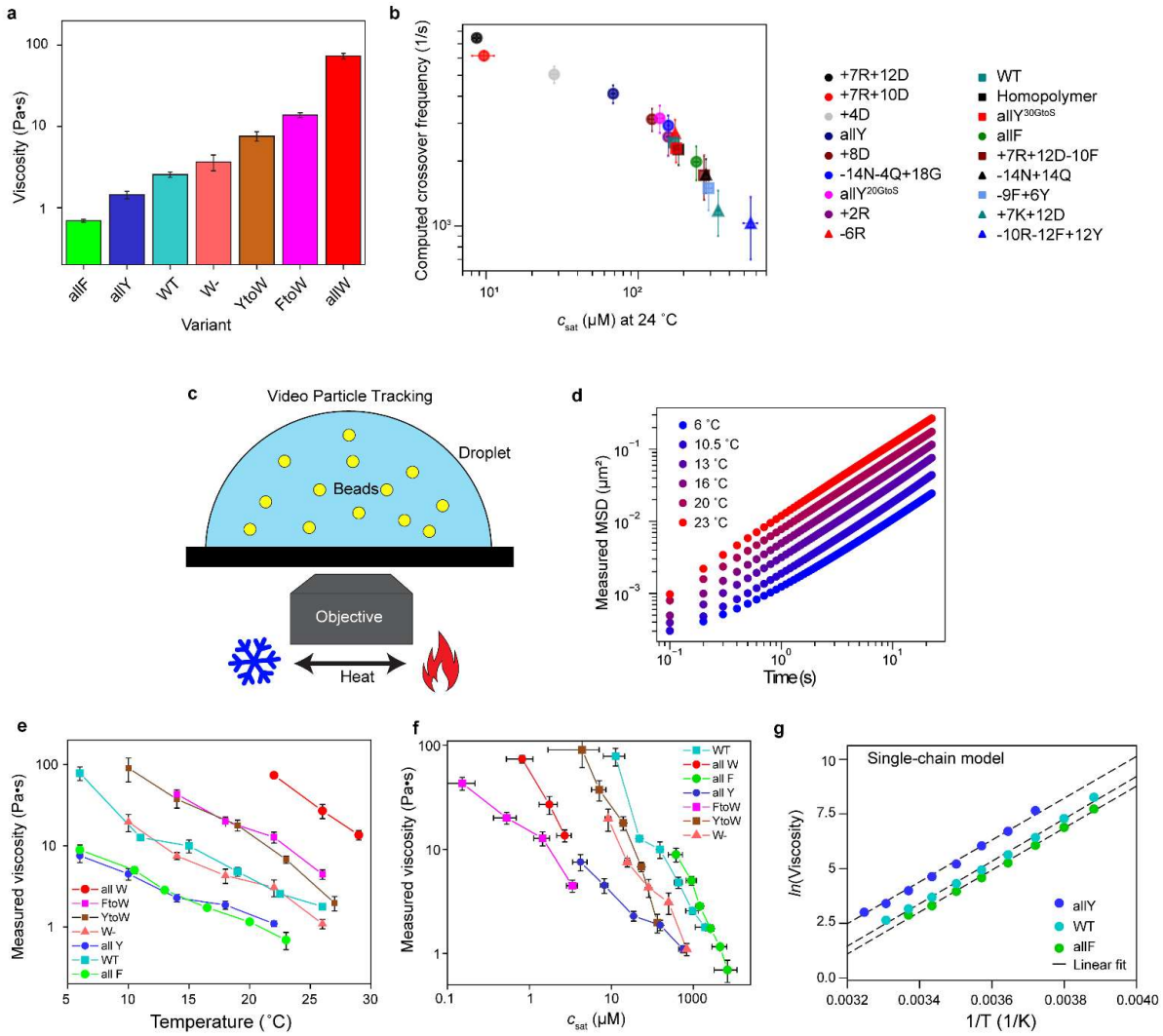

ED Fig. 3. (a) Room-temperature viscosity of condensates formed by different sequence variants of A1 LCD as measured by video particle tracking. Data is collected from at least five trials featuring at least ~50 tracked particles per trial. Error bars represent ±1 standard deviation. **(b)** Computed crossover frequencies were calculated by analyzing simulation results using the collective model. The results are plotted against the c_{sat} values computed at room temperature. The crossover frequency is the inverse of the network reconfiguration time of the respective condensate. **(c)** Schematic for the temperature-dependent video particle tracking experiment. Diffusion of multiple 200 nm polystyrene beads is recorded at distinct temperatures. **(d)** Representative plots of the ensemble-averaged MSD of 200 nm polystyrene beads within condensates formed by allF. Measurements were made using video particle tracking microrheology at different temperatures as set by a custom-made thermal stage attached to the microscope. **(e)** Measured temperature-dependent viscosities for the condensates formed by different sequence variants of A1 LCD used for the Arrhenius plots in Fig. 2c. **(f)** Measured temperature-dependent viscosities for condensates formed by different variants plotted against the temperature-dependent c_{sat} values. **(g)** Arrhenius plots for viscosities calculated from analysis of simulation results using the single-chain model.

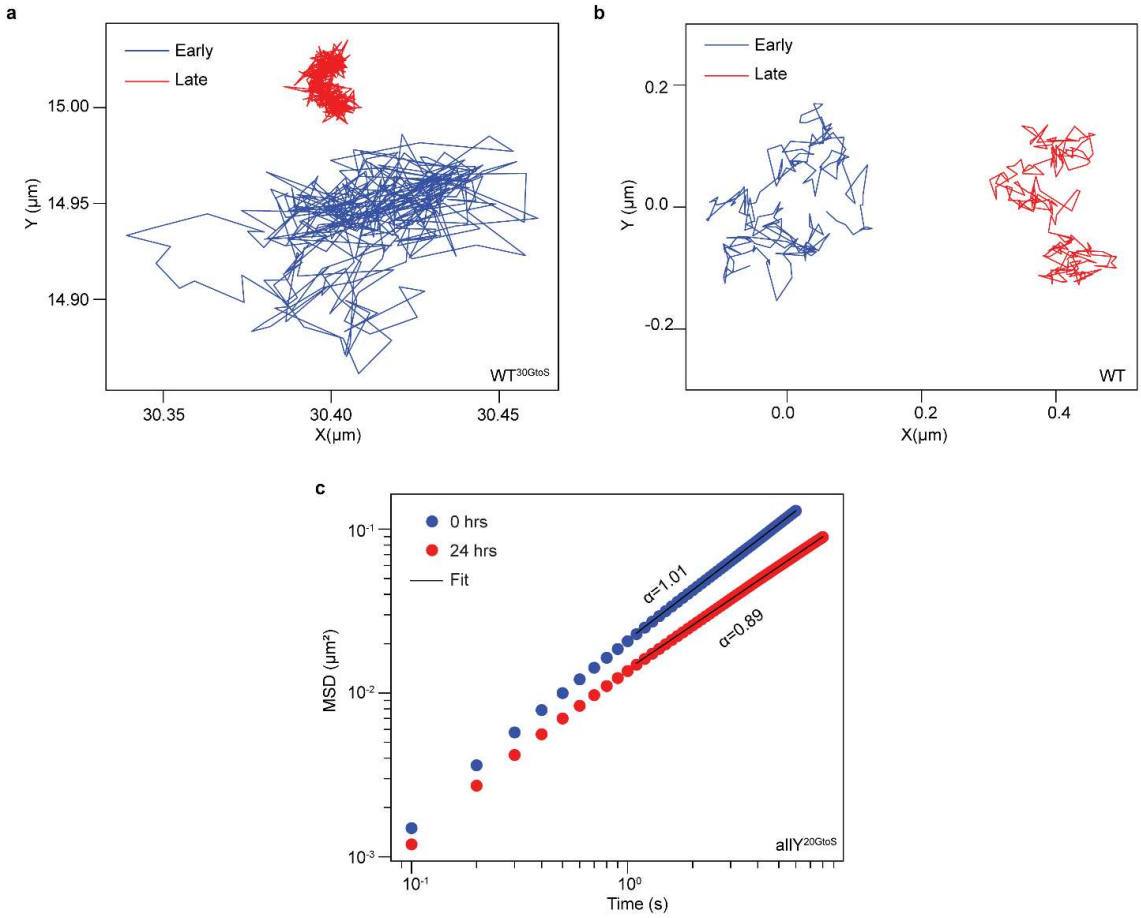

ED Fig. 4. (a) Trajectory of a 200 nm bead within freshly prepared condensate of WT^{30GtoS} variant of A1 LCD (blue) and approximately 2 minutes after the start of imaging (red). These data show that WT^{30GtoS} condensates undergo dynamical arrest within a short timescale. **(b)** Same as **(a)** but for WT A1 LCD condensate. **(c)** Ensemble-averaged MSD of 200 nm beads in fresh (0 hrs) or aged (24 hrs) condensates formed by $allY^{20GtoS}$. Solid lines are the fits to the equation $MSD(\tau) = 4D\tau^{\alpha} + N$. Also indicated are the values of the diffusivity exponent obtained from the fits, which show a clear deviation from the linear behavior for the aged condensates, indicating sub-diffusive motion of the probe particles.

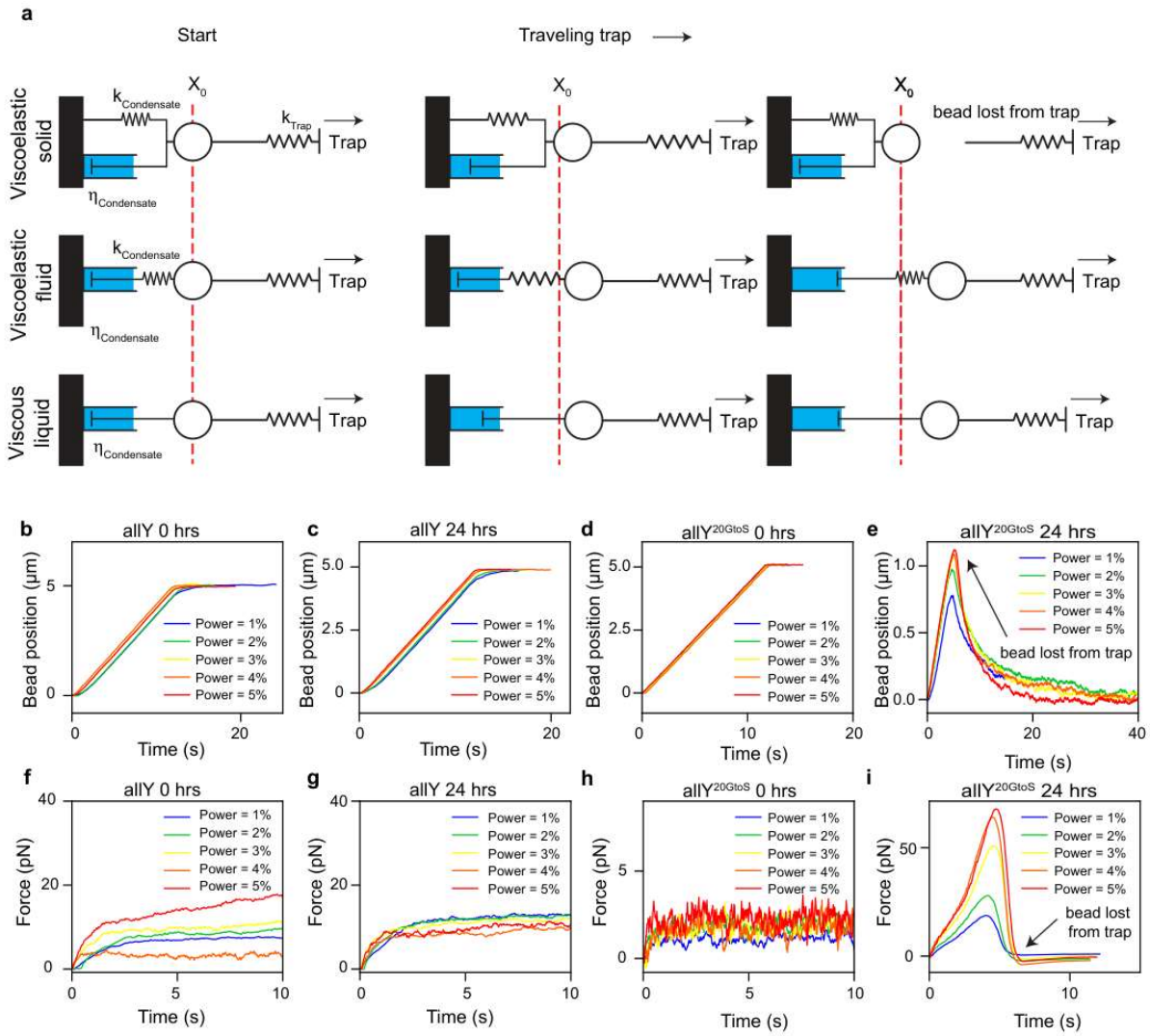

ED Fig. 5. (a) A schematic showing the expected outcomes of a particle embedded within a viscoelastic Kelvin-Voigt solid (top), viscoelastic Maxwell fluid (middle), and viscous liquid (bottom) upon creep deformation by an optical trap. As the optical trap exerts a force to drag a particle embedded within the fluid medium, the dashpot element applies a dissipative drag force while the spring element applies a restoring force. Except for the viscoelastic solid, the creep deformation is irreversible (the final bead position is distinct from the initial bead position X_0, indicated by the red vertical line). In the case of a viscoelastic solid, the bead recoils back to its initial position due to the stored energy within the elastic spring. In both viscoelastic fluids and viscous liquids, the deformation energy is eventually dissipated through the dashpot or the viscous element, giving rise to a terminally viscous behavior. **(b)** Bead position as a function of time in response to the programmed trap movement in nascent allY condensates at increasing power levels of the trapping laser. **(c)** Same as (**b**) but for the allY condensates after 24 hours following sample preparation. **(d)** Bead position as a function of time in response to the programmed trap movement in nascent allY^{20GtoS} condensates at increasing power levels of the trapping laser. **(e)** Same as (**d**) but for the allY^{20GtoS} condensates after 24 hours. **(f)** The force exerted on the bead by the allY condensate network in (**b**). **(g)** The force exerted on the bead by the allY condensate network in

(**c**). **(h)** The force exerted on the bead by the allY^{20GtoS} condensate network in (**d**). **(i)** The force exerted on the bead by the allY^{20GtoS} condensate network in (**e**).